Noname manuscript No.
(will be inserted by the editor)

$\gamma n(p) \to \pi^- p(p)$ asymmetries with linearly polarized beam and longitudinally polarized targets in the N* Resonance Region

H. Y. Lu for the g14 Analysis Group and the CLAS Collaboration

Received: date / Accepted: date

Abstract The excited-state spectrum of the nucleon is a complicated overlap of many resonances that must be disentangled through multipole analyses of reaction amplitudes. Meson photoproduction, which has been a fruitful probe of N* structure, requires data on many different polarization observables to constrain its four complex amplitudes. While considerable data has been accumulated with proton targets, comparatively little information is available from neutron targets. Recently, the first beam-target helicity asymmetries with circular beam polarization in the $\gamma n(p) \to \pi^- p(p)$ reaction have been reported [1]. This talk presents a parallel analysis from the same experiment of the beam-target double-polarization observable "G" with linearly polarized beam for the same reaction. Linearly polarized photons and longitudinally polarized deuterons in a solid hydrogen deuteride (HD) target were used with the CEBAF Large Acceptance Spectrometer (CLAS) at Jefferson lab (JLab). Data are combined to extract the beam (Σ) and beam-target (G) asymmetries. Preliminary results for the Σ observables are consistent with existing partial wave analyses (PWA) that incorporate other experiments. Preliminary results for the energy and angular dependence of G are reported; these deviate strongly from existing PWA.

Keywords meson photoproduction · polarization · polarized targets · Baryon resonances

PACS 25.20.Lj · 13.88.+e · 14.20.Gk

1 Introduction

Quantum Chromodynamics (QCD) is widely accepted as a successful theory to describe the strong interaction. However, the spectrum of nucleon excita-

H. Y. Lu
University of Iowa
E-mail: hlu@jlab.org

tion resonances (N*) poses many challenges. These range from the predictions of as yet unobserved levels to understanding the properties of well-established states. In addition, the spectral properties are altered by "dressing", such as meson loops and channel couplings [2], which are beyond the scope of perturbative QCD (pQCD) . Although πN scattering data has been intensively analyzed to extract the information on N*s, a complete decomposition of the reaction amplitude into multipoles of definite isospin, spin, and parity has not been achieved. Furthermore, comparatively little information from neutron target reactions is available, while it is required to separate γpN^* and γnN^* couplings and deduce the isospin $I = 1/2$ amplitudes. Single pseudo-scalar meson production, such as π production, requires data on a minimum of 8 out of a total 16 different spin observables to avoid mathematical ambiguities [3]. This work is aiming to provide 2 of them in N* resonance region.

The E06-101 experiment (the g14 run) at Jefferson Lab with the CEBAF Large Acceptance Spectrometer (CLAS) in Hall B [4], utilized a polarized beam on a polarized HD target [5–7]. During the experiment, both circularly-polarized and linearly-polarized photons were generated by the bremsstrahlung of either polarized electrons or by the use of a diamond radiator, respectively. The first beam-target helicity asymmetries with circular beam polarization in the $\gamma n(p) \to \pi^- p(p)$ reaction were reported recently in ref. [1]. In this work, only reactions produced by linearly-polarized photons were analyzed, and the beam (Σ) and beam-target (G) helicity asymmetries were extracted over the same energy reaction.

2 Separating asymmetries with double-polarization data

The general expression for the single pseudoscalar-meson production cross section involving a linear polarized beam and a longitudinal polarized target (summed over final recoil polarization states) is [3]:

$$\frac{d\sigma(P_\gamma,P_D)}{d\Omega} = \frac{d\sigma_0}{d\Omega}\left(1 - P_\gamma^L \Sigma(\theta;W)cos(2\phi) + P_\gamma^L P_D^V G(\theta;W)sin(2\phi)\right), \quad (1)$$

where σ_0 is a constant independent of beam or target polarization, P_γ^L is the degree of beam linear polarization, $P_D{}^V$ is the vector polarization of the deuteron along the beam axis Z, and ϕ is the azimuthal angle relative to the electric vector of the photon; Σ and G are beam and beam-target asymmetries, respectively. The linear beam polarization plane is either X-Z plane or Y-Z plane. Suppose for an arbitrary detector element, the azimuthal angle is ϕ relative to X-Z plane. Then its azimuthal angle relative to Y-Z plane is $\pi/2 + \varphi$ The $cos(2\phi)$ term in Eqn. 1 will give opposite signs for these cases. The target polarization is either +Z or -Z. The P_D^V term will give two opposite signs. All combinations of beam polarization and target polarization give four configurations: 1. beam polarization at 0 degree and target polarization at +Z direction; 2. beam at 0 degree and target at -Z; 3. beam at 90 degree and target at +Z; 4. beam at 90 degree and target at -Z. The yields of these four configurations at a certain angle are:

$$\begin{aligned}
Y_1 &= L_1 A \Delta\Omega \frac{d\sigma_0}{d\Omega} \left(1 - p_1 \Sigma cos(2\phi) + p_1 p_+ G sin(2\phi)\right) \\
Y_2 &= L_2 A \Delta\Omega \frac{d\sigma_0}{d\Omega} \left(1 - p_2 \Sigma cos(2\phi) - p_2 p_- G sin(2\phi)\right) \\
Y_3 &= L_3 A \Delta\Omega \frac{d\sigma_0}{d\Omega} \left(1 + p_3 \Sigma cos(2\phi) + p_3 p_+ G sin(2\phi)\right) \\
Y_4 &= L_4 A \Delta\Omega \frac{d\sigma_0}{d\Omega} \left(1 + p_4 \Sigma cos(2\phi) - p_4 p_- G sin(2\phi)\right),
\end{aligned} \tag{2}$$

where L_i is the luminosity for each configuration, A is the acceptance which is approximately the same for all the configurations when $\Delta\Omega$ the solid angle of each bin is large enough, p_i is the average beam polarization of each configuration, p_+ and p_- are target polarization along the +Z and -Z direction. By using simple algebra, terms in Σ and in G can be evaluated independently as:

$$\begin{aligned}
\Sigma cos(2\phi) &= \frac{s_1 Y_1 + s_2 Y_2 + s_3 Y_3 + s_4 Y_4}{a_1 Y_1 + a_2 Y_2 + a_3 Y_3 + a_4 Y_4} \\
G sin(2\phi) &= \frac{g_1 Y_1 + g_2 Y_2 + g_3 Y_3 + g_4 Y_4}{a_1 Y_1 + a_2 Y_2 + a_3 Y_3 + a_4 Y_4},
\end{aligned} \tag{3}$$

where the coefficients for Σ are:

$$\begin{aligned}
s_1 &= \frac{-(p_-)p_2 C_0}{N_1} \\
s_2 &= \frac{-(p_+)p_1 C_0}{N_2} \\
s_3 &= \frac{(p_-)p_4 C_{90}}{N_3} \\
s_4 &= \frac{(p_+)p_3 C_{90}}{N_4} \\
a_1 &= \frac{p_- D}{N_1 p_1} \\
a_2 &= \frac{p_+ D}{N_2 p_2} \\
a_3 &= \frac{p_- D}{N_3 p_3} \\
a_4 &= \frac{p_+ D}{N_4 p_4},
\end{aligned} \tag{4}$$

where N_i is the product of some constant with L_i and

$$\begin{aligned}
C_0 &= p_4 p_- + p_3 p_+ \\
C_{90} &= p_2 p_- + p_1 p_+ \\
D &= p_1 p_2 p_3 p_4.
\end{aligned} \tag{5}$$

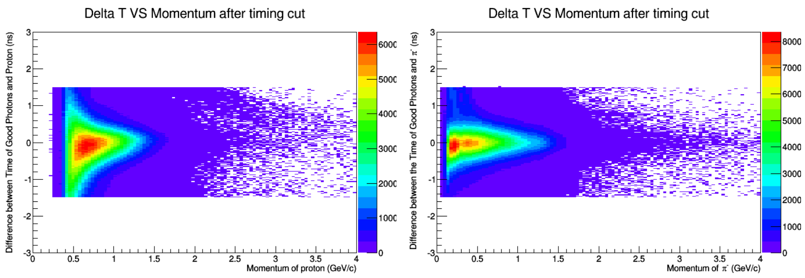

Fig. 1 Time difference between Proton (left) or π^- (right) and photon VS their momenta respectively.

The normalization factors N_i are extracted from the reconstructed reaction yields originating in a foil that is independent of the target (see Sect. 3.4). It is convenient to express the coefficients for G in terns of a new variable, defined as:

$$E = (p_1 + p_3)p_2p_4p_- + (p_2 + p_4)p_1p_3p_+. \tag{6}$$

Then the coefficients for G are:

$$\begin{aligned} g_1 &= \frac{Ep_2}{N_1} \\ g_2 &= \frac{Ep_1}{N_2} \\ g_3 &= \frac{Ep_4}{N_3} \\ g_4 &= \frac{Ep_3}{N_4}. \end{aligned} \tag{7}$$

With these coefficients evaluated for four different sets of run conditions, Σ and G can be extracted independently from equation (3) by fitting $cos(2\phi)$ and $sin(2\phi)$ distribution.

3 Event Selection, Cuts and Corrections

To minimize the statistical and systematical uncertainties simultaneously, a series of data selection cuts have been applied and checked. There are four major cuts and one correction that has been applied in this work. They are described in this section.

3.1 Timing Requirements

In each event, timing and energy information of many photons are recorded. However, only one photon generates the event. In order to find the correct photon and discard the events where no correct photon information can be found, a timing cut is applied.

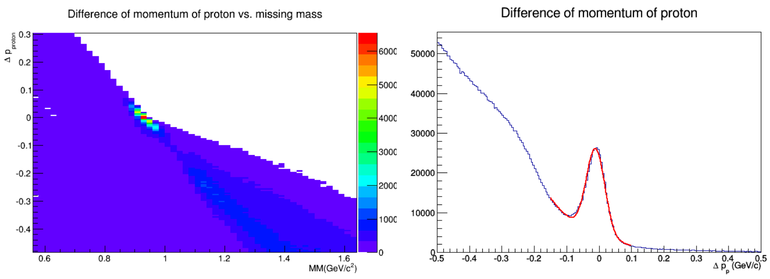

Fig. 2 Left: difference between measured momentum and theoretical momentum of proton VS missing mass; right: fit of the difference with a polynomial background and a Gaussian peak. (See section 3.2 .)

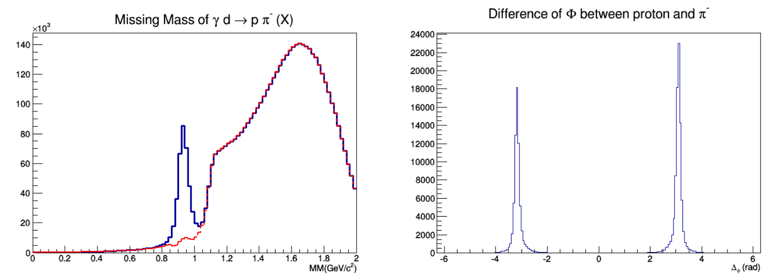

Fig. 3 Left: missing mass before selection (blue) and cut away(red); right: ϕ angle between proton and π^-.

First, the events of two and only two reconstructed charged particles are selected. The positive charged particle is assumed to be proton, and the negative charged is assumed to be a π^-. The two times when these two particles are at the target center are calculated from the tracking length, the hit time at the time-of-flight counters, and from the momentum for each particle. These are com-pared with the photon time at the target center. Figure 1 shows the difference between the times of protons (left) or π^- (right) and photons. The cut is ap-plied on both of the time differences and requires $\pm 1.5ns$. Every event with a selected photon is consistent with the assumption that a photon reacts in the target and generates a proton and a π^- with consistent timing.

3.2 Exclusivity Requirements

In Sect. 3.1, only the timing information is considered. The missing mass after the above cut is shown in blue on the left side of Fig. 3. The peak at 0.9 GeV/c^2 is mainly from a spectator proton. The events other than the peak are from either inclusive production of $p\pi^-$ or other production channel whose timing is accidentally coincident. In order to select the events from the exclusive $p\pi^-$ production, an exclusive cut is performed using the following steps.

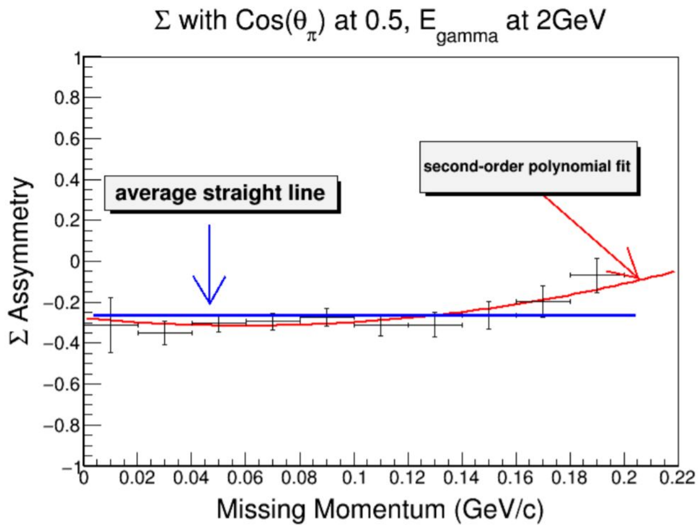

Fig. 4 Σ with different missing momentum selections.

1. Calculate the boost needed to reach the center-of-mass frame of the photon and a neutron with non-zero momentum. The momentum of the neutron is calculated from the detected proton and π^- by assuming a two-body reaction and momentum conservation.
2. Calculate the momentum of the proton in the above center-of-mass frame, p_1, by assuming the two-body reaction $\gamma n \to p\pi^-$.
3. Boost the detected proton momentum (p_2) into this center-of-mass frame and calculate the difference $\Delta p = p_1 - p_2$. This Δp is shown versus missing mass at the left in Fig. 2. The exclusive production events are concentrated in the area with y-coordinate around 0 and x-coordinate right below 1 GeV/c^2.
4. The distribution of Δp is shown at the right in Fig. 2. A polynomial background plus a Gaussian-distribution peak is used to obtain the red curve. A 3-σ cut is applied to select the events.

The exclusivity cut is very efficient. Figure 3 shows the missing mass of *cut-away* events (those outside the above 3σ selection) in red at the left, and the azimuthal angle between proton and π^- at the right. In the missing mass plot, it is clear that the cut-away distribution (red) is consistent with the background of all events (blue) before the cut. It leaves a set of very pure exclusive production events for the next steps of analysis. The azimuthal angle difference distribution confirms this by displaying two isolated peaks at $\pm$ 180 degrees, which is consistent with the two-body reaction assumption.

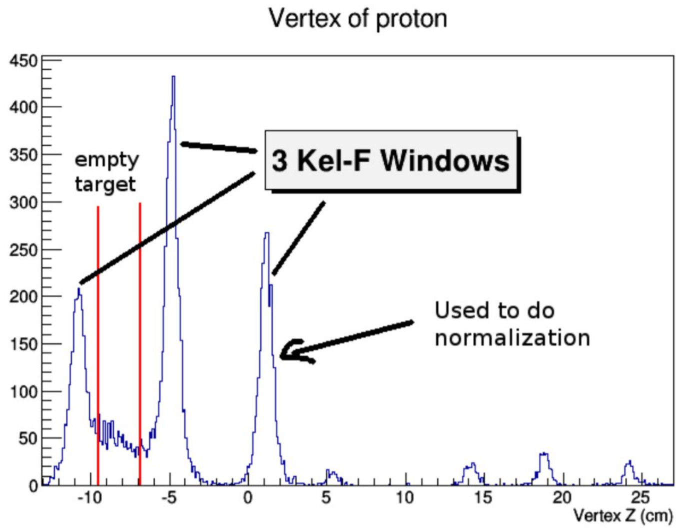

Fig. 5 Vertex distribution of an empty target.

3.3 Missing Momentum Requirement

As the momentum of the undetected proton in the $p\pi^-(p)$ final state increases, the potential grows for contributions from complex final state interactions (FSI), which are not associated with the effective γ+n process of interest. While this favors a tight cut on the missing momentum, it comes at the cost of statistical uncertainty. Rather than invoking theoretical arguments, we have let the data itself determine the optimal maximum momentum. The missing momentum dependence of Σ is shown in Fig. 4. Σ values are essentially independent of missing momentum below 0.18 GeV/c, beyond which they begin to rise. A second-order polynomial function extrapolates the value at zero-missing momentum, which is very close to the average value. A maximal missing momentum of 0.2 GeV/c has been adopted for the results discussed here.

3.4 Dilution Factor and Reaction Vertex Requirement

Figure 5 shows the vertex distribution from an empty target. There are three dominant peaks from Kel-F (C_2ClF_3) windows. Between the first two Kel-F windows, there exist auxiliary aluminum cooling wires (and target material when a cell full of HD is used). The third major peak is isolated from target area and provides the opportunity to flux-normalize runs of different polarization configurations, as well as between empty target runs and production runs. The target material area is defined as from -9.6 to -6.9 cm (red lines in Fig. 5). Events inside the target material area are finally chosen to extract asymmetries.

The aluminum within the target material area of figure 5 is not polarized and cannot contribute to the

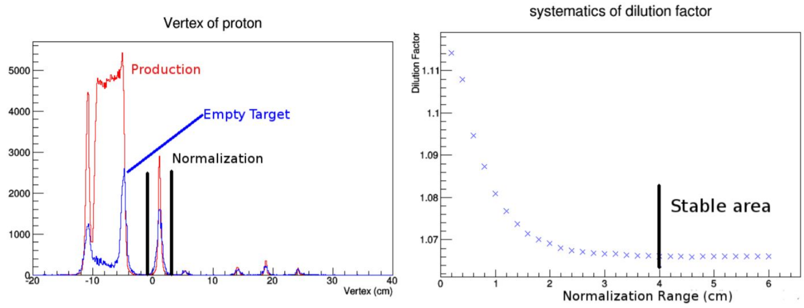

Fig. 6 Left: production vertex distribution in red and empty target in blue; right: dilution factor dependence on the width of normalization area.

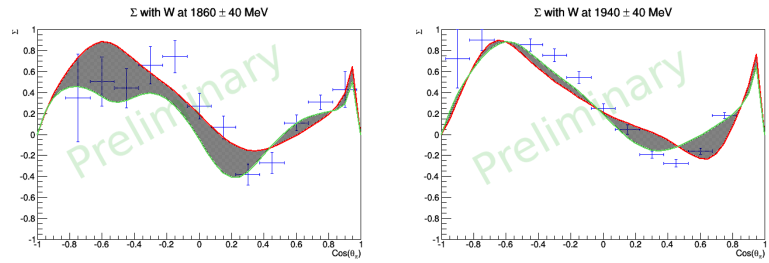

Fig. 7 Σ dependence on $cos(\theta_\pi)$ with SAID model prediction. Points with error bar are from this work for the W ranges from 1820 to 1900 MeV (left), and from 1900 to 1980 MeV (right). The shadow areas are the SAID predictions bounded by the upper and lower limits of the invariant mass interval.

asymmetries. Therefore, they dilute the asymmetry values and need to be corrected. The dilution factor is defined as:

$$f_{dilution} = \frac{N_p}{N_p - N_e} \tag{8}$$

where N_p and N_e are number of flux-normalized events in the target material area from production target and empty target runs respectively. This dilution factor is a correction which multiplies the extracted asymmetry values. The production vertex distribution (red) is shown together with empty-target data (blue) on the left of Fig. 6. They are normalized by matching the number of events in the normalization area around the third Kel-F peak. The normalization area is determined by the width around the third peak, as indicated by two straight vertical lines. After varying this width, the dilution factor varies as shown on the right side of Fig. 6. When the width is greater than 4 cm, the value is stable. The final value is taken as the average of the stable values, namely 1.066.

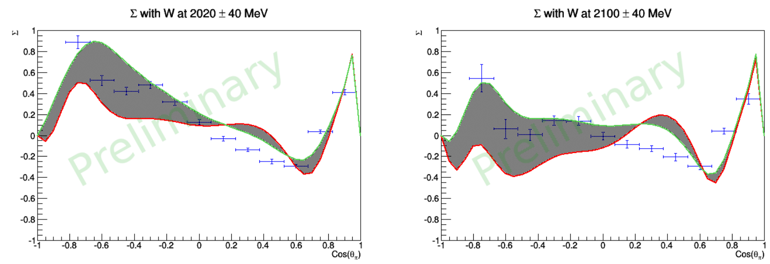

Fig. 8 Σ dependence on $cos(\theta_\pi)$ with SAID model prediction. Points with error bar are from this work for the W range from 1980 to 2060 MeV (left) and from 2060 to 2140 MeV (right). Shadow areas are as in figure 7.

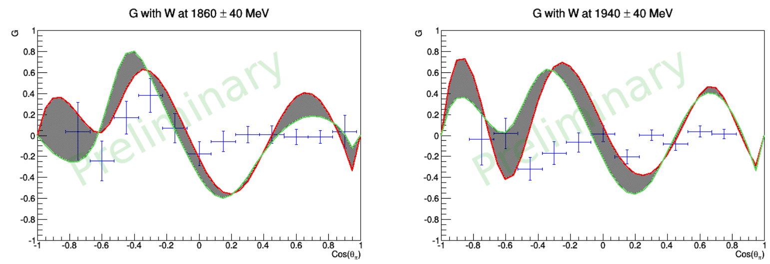

Fig. 9 G dependence on $cos(\theta_\pi)$ with SAID model prediction. Points with error bar are from this work for the W range from 1820 to 1900 MeV (left) and from 1900 to 1980 MeV (right). Shadow areas are as in figure 7.

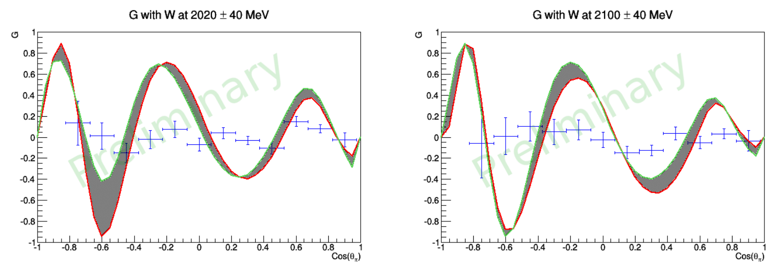

Fig. 10 G dependence on $cos(\theta_\pi)$ with SAID model prediction. Points with error bar are from this work for the W range from 1980 to 2060 MeV (left) and from 2060 to 2140 MeV (right). Shadow areas are as in figure 7.

4 results

After the events pass through all the selection criteria, Σ and G are separated by using the method described in Sect. 2. The results of Σ are shown in Figs. 7 and 8, while the results of G are in Figs. 9 and 10. The predictions of the SAID partial wave analysis (PWA) are compared with the results. (These SAID PWA have not yet been fitted to these new asymmetry results.) The shaded areas are the PWA prediction for the corresponding W range. As shown, the Σ results have a very good agreement with the model prediction, while the G results are generally very much smaller than the model predicted values. Because of these large differences, we expect these new G results to have a significant impact on future PWA, and through them on the determination of N* resonance parameters.

Acknowledgements

This work was supported by the U.S. Department of Energy, Office of Nuclear Physics Division, under Contract No. DE-AC05-06OR23177, under which Jefferson Science Associates operate Jefferson Laboratory, by the US National Science Foundation, and by the funding agencies of CLAS collaboration members.

References

1. D. Hao *et al.*, Beam-Target Helicity Asymmetry for $\boldsymbol{\gamma}\mathbf{n} \to \pi^- p$ in the N^* Resonance Region, PRL, 118, 242002 (2017)
2. N. Suzuki *et al.*, Disentangling the Dynamical Origin of P_{11} Nucleon Resonances, PRL, 104, 042302 (2010)
3. A. M. Sandorfi *et al.*, Determining pseudoscalar meson photoproduction amplitudes from complete experiments, J. of Phys. G, 38, 053001 (2011)
4. B. A. Mecking *et al.*, The CEBAF Large Acceptance Spectrometer (CLAS), Nucl. Instrum. Meth. A, 503, 513 (2003)
5. C. D. Bass *et al.*, A Portable Cryostat for the Cold Transfer of Polarized Solid HD Targets: HD-Ice-I, Nucl. Instrum. Meth. A, 737, 107 (2014)
6. M. M. Lowry *et al.*, A Cryostat to Hold Frozen-Spin Polarized HD Targets in CLAS: HDice-II, Nucl. Instrum. Meth. A, 815, 31 (2016)
7. X. Wei *et al.*, Boosting Deuteron Polarization in HD Targets: Experience of moving spins between H and D with RF methods during the E06-101 experiment at Jefferson Lab, PoS, PSTP2013, 016 (2014)